ACS APPLIED MATERIALS & INTERFACES

Research Article

www.acsami.org

Synthesis of Amorphous FeOOH/Reduced Graphene Oxide Composite by Infrared Irradiation and Its Superior Lithium Storage Performance

Yongming Sun, Xianluo Hu,* Wei Luo, Henghui Xu, Chenchen Hu, and Yunhui Huang*

State Key Laboratory of Materials Processing and Die & Mould Technology, School of Materials Science and Engineering, Huazhong University of Science and Technology, Wuhan 430074, China

Supporting Information

ABSTRACT: A new hybrid nanostructure composed of mildly reduced graphene oxide (mRGO) nanosheets and homogeneous loading of amorphous FeOOH with ultrafine particles (~2 nm) is successfully synthesized via a facile infrared irradiation approach. Surprisingly, the as-prepared FeOOH/mRGO hybrid exhibits high reversible capacity, long-term stability, and excellent rate performance, when used as an anode material for lithium-ion batteries. A high reversible capacity of 767 mA h g^{-1}, with a coulombic efficiency of ~100%, can be achieved at a high current density of 1000 mA g^{-1} even after 600 discharge/charge cycles. The superior electrochemical performances are attributed to the synergistic effects of the small particle size, amorphous structure, and conductive mRGO.

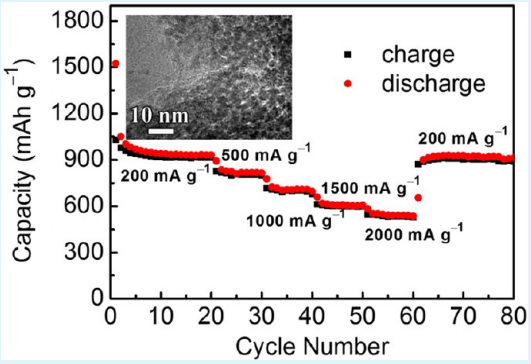

KEYWORDS: *FeOOH, MRGO, infrared irradiation, lithium storage performance*

INTRODUCTION

Rechargeable lithium-ion batteries are the key parts of portable electronic devices, electric/hybrid electric vehicles, and the storage of renewable energy.[1−4] Graphite, the mostly commonly commercial anode material, cannot meet the ever-increasing demand for high-performance lithium-ion batteries because of its low theoretical specific capacity (372 mA h g^{-1}) and limited rate capability.[5] It is highly challenging but desirable to develop novel anode materials with larger capacities and higher lithium diffusion rates.[3] Fabricating various carbonaceous nanocomposites and nanostructures seems to be the most applicable strategies.[6−14] Graphene, a two-dimensional carbon material, has attracted much interest in the fields of energy-storage applications because of its high surface area, superior electrical conductivity, chemical stability and excellent mechanical flexibility,[15−19] Up to now, many graphene-based hybrid anodes have been prepared,[20−24] and they indeed exhibit enhanced electrochemical performances compared to their bare counterparts. Besides, the preparation of nano-architectures with amorphous structure has been reported to be an effective route to obtain fast lithium insertion/extraction kinetics and long lifespan.[25−28]

In recent years, iron oxides/hydroxides (e.g., Fe_2O_3, Fe_3O_4, and FeOOH) as anode materials for lithium-ion batteries have aroused much attention because of their low cost, nontoxicity, and high capacity.[29−37] Various nanostructured Fe_2O_3 and Fe_3O_4 are explored and exhibit enhanced capacity and cyclability.[29−33] In contrast, FeOOH is rarely studied because of insulating nature and unstability. Zhang et al. reported that α-FeOOH can uptake and extract a large amount of Li via the conversion reaction mechanism.[35] Tabuchi et al. reported that a β-FeOOH film anode can deliver a high initial capacity of 846 mA h g^{-1}.[36] Nevertheless, the cycle life of FeOOH-based anodes is limited because of the low conductivity and large volume change during the uptake/release of lithium.[35,36] To meet the ever-increasing energy demand, therefore, it is highly desirable but challenging to develop high-capacity and long-lifespan FeOOH-based anode materials.

In this work, we report on a novel infrared irradiation approach to synthesize amorphous FeOOH with ultrafine particles (~2 nm) grown on mRGO nanosheets. Because of advantageous combination of ultrafine nanoparticles, amorphous structure and conductive mRGO, the as-prepared hybrid exhibits high reversible capacity, excellent rate capability, and long cycle life when evaluated as an anode material for lithium-ion batteries.

EXPERIMENTAL SECTION

Materials Synthesis. Firstly, GO was obtained by the modified Hummers method.[38,39] Then the as-prepared GO was mildly reduced using hydrazine hydrate as a reducing agent. Namely, the as-prepared GO (100 mg) was dispersed in water (100 mL) by sonication. The hydrazine hydrate (1.0 mL, 32.1 mmol) was then added. This suspension was heated in an oil bath at 90 °C for 6 h, and mRGO was

Received: July 16, 2013
Accepted: September 25, 2013
Published: September 25, 2013

finally obtained. For synthesis of amorphous FeOOH/mRGO composite, a facile infrared irradiation method was explored. In a typical procedure, 100 mg of mRGO was dispersed in 50 mL of deionized (DI) water under sonication for 1 h to form a homogenous suspension. Then, 2 mmol of iron(III) nitrate nonahydrate (0.8080 g) was added directly into the suspension under stirring. The mixed suspension was heated in an oil bath at 70 °C until thick slurry formed. Finally, the FeOOH/mRGO composite was obtained after treatment of the resulting slurry under infrared irradiation for 2 h. For comparison, bare FeOOH was also prepared under the same condition with a further heat treatment at 160 °C in air for 1h.

Materials Characterization. The phase of the products was identified using a powder X-ray diffraction (XRD) diffractometer (X'Pert PRO, PANalytical B.V., Holland) with Cu $K_{\alpha 1}$ irradiation (λ = 1.5406 Å). The chemical state of the products was studied by X-ray photoelectron spectroscopy (XPS) using a VG MultiLab 2000 system (Thermo Scientific). The photoelectrons are excited using a monochromatic Al K_α X-ray source. The morphology was observed by field-emission scanning electron microscopy (FESEM, FEI Sirion 200), which is coupled with an energy-dispersive X-ray (EDX) spectrometer (Oxford Intrument) for composition analysis. Transmission electron microscopy (TEM, JEOL 2100F) was used to investigate the microstructure of the products. Raman spectra were recorded using a Renishaw Invia spectrometer. The source of irradiation is an Ar^+ laser of 514.5 nm operating at room temperature. Thermogravimetric (TG) data were obtained on a TG analyzer (PerkinElmer Diamond) at 10 °C min^{-1} in air.

Electrochemical Measurement. The working electrode was made of the as-prepared FeOOH/mRGO hybrid (or bare FeOOH), acetylene black (Super P), and polyvinylidene fluoride (PVDF) as a binder (80:10:10, weight ratio). The coin cells (2032-type) consisted of a lithium foil as the counter electrode, a membrane (Celgard 2300) as the separator, and 1 M $LiPF_6$ in ethylene carbonate (EC) and dimethyl carbonate (DMC) (v/v = 1:1) as the electrolyte. Cyclic voltammetry (CV), electrochemical impedance spectrometry (EIS), and galvanostatic charge/discharge measurements were carried out according to ref 20.

RESULTS AND DISCUSSION

Figure 1 shows a schematic illustration for the formation of the FeOOH/mRGO composite. In a typical procedure, an iron(III)

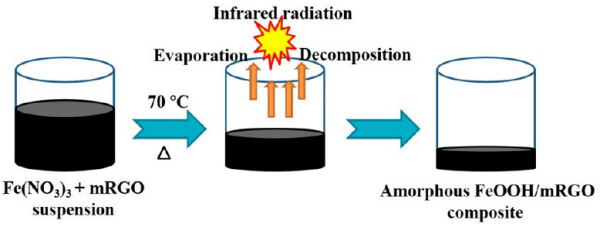

Figure 1. Schematic illustration for the formation of the FeOOH/mRGO composite.

nitrate/mRGO suspension was slowly dried and transformed to the sticky slurry during the solvent vaporization. The FeOOH nanoparticles were then gradually deposited and embedded in the mRGO network under infrared irradiation. Figure 2a displays the typical XRD pattern of the resulting FeOOH/mRGO product that was obtained after infrared irradiation. No obvious diffraction peaks were observed, confirming the amorphous structure of the as-prepared material. A typical survey XPS spectrum for the as-prepared FeOOH/mRGO composite was shown in Figure 2b, indicating the existence of Fe, O, and C. The peaks of Fe (Fe 2s, $2p_{1/2}$, $2p_{3/2}$, LMM, 3p) and O (O 1s, KLL) can be assigned to characteristic of FeOOH.[40] Figure 2c displays the high-resolution XPS spectrum

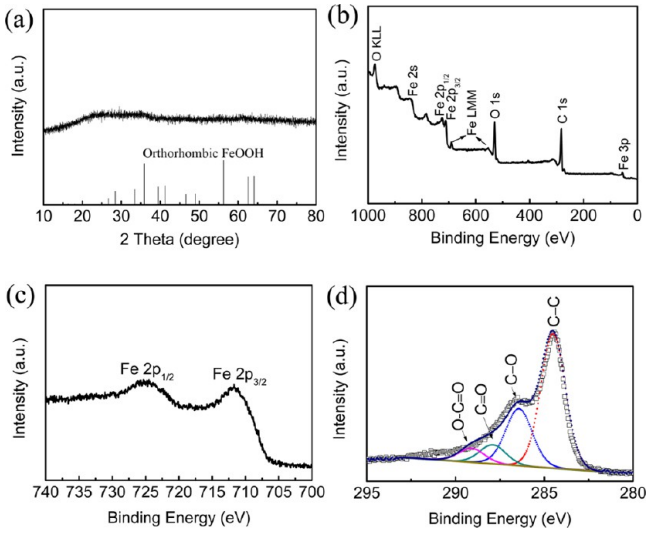

Figure 2. (a) Representative XRD pattern of the amorphous FeOOH/mRGO hybrid. XPS spectra of the FeOOH/mRGO hybrid: (b) survey XPS spectrum and high-resolution of (c) Fe 2p and (d) C 1s spectra.

of Fe 2p. Two main peaks at 725.0 and 711.4 eV were found, corresponding to the Fe $2p_{1/2}$ and Fe $2p_{3/2}$ spin-orbit peaks of FeOOH.[40] The peak of C 1s arises from mRGO, and the high-resolution C 1s spectrum is shown in Figure 2d. It can be well fitted into four peaks that are attributed to carbon atoms from different oxygen-containing functional groups. The strong C 1s peak at 284.5 eV corresponds to graphitic carbon in mRGO, whereas the other three peaks at higher binding energies arise from the oxygenated carbons: C−O (286.4 eV), C═O (287.9 eV), and O−C═O (289.0 eV).[41] Compared with those of the RGO-based composites,[20,42−44] these peaks show much higher relative intensity, indicating the existence of much more oxygen-containing functional groups in the mRGO of the resulting composite. Figure S1 in the Supporting Information shows the high-resolution XPS spectrum of O 1s for the FeOOH/mRGO composite. The O 1s peak at 530.0 eV may arise from Fe^{3+} in FeOOH.[40] Also, there appears a small peak at 532.6 eV for O 1s, indicating that oxygen-containing groups bonded with C atoms exist in mRGO.[41]

The general morphology of the as-obtained material was investigated by FESEM. Figure 3a shows the low-magnification FESEM image of the FeOOH/mRGO composite. There exist a large number of micrometre lateral dimension nanosheets in the product. FESEM observations at a higher magnification (Figure 3b) reveal that the surface of these nanosheets is much rougher in comparison with that of the bare mRGO (see Figure S2 in the Supporting Information). This indicates that a thin nanostructured layer of FeOOH has been successfully grown on the surface of the mRGO. The elemental composition of the product was probed by EDX analysis (see Figure S3 in the Supporting Information). The results indicate that the as-prepared sample is composed of Fe, O, and C, which is consistent with the XPS results (Figure 2b−d). In addition, the EDX elemental mappings indicate the uniform distribution of Fe, O and C in the FeOOH/mRGO composite (see Figure S4 in the Supporting Information). Additionally, the chemical composition of the bare FeOOH product was determined by EDX (see Figure S5 in the Supporting Information). The atomic ratio of O to Fe is evaluated to be about 1.98:1, consistent well with that of FeOOH. Raman spectroscopy is an

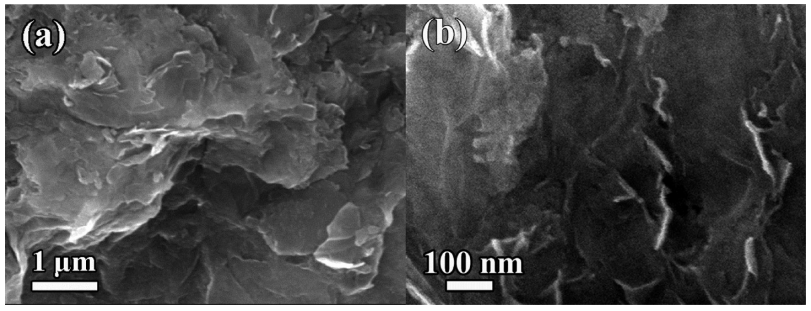

Figure 3. FESEM images of the obtained FeOOH/mRGO hybrid.

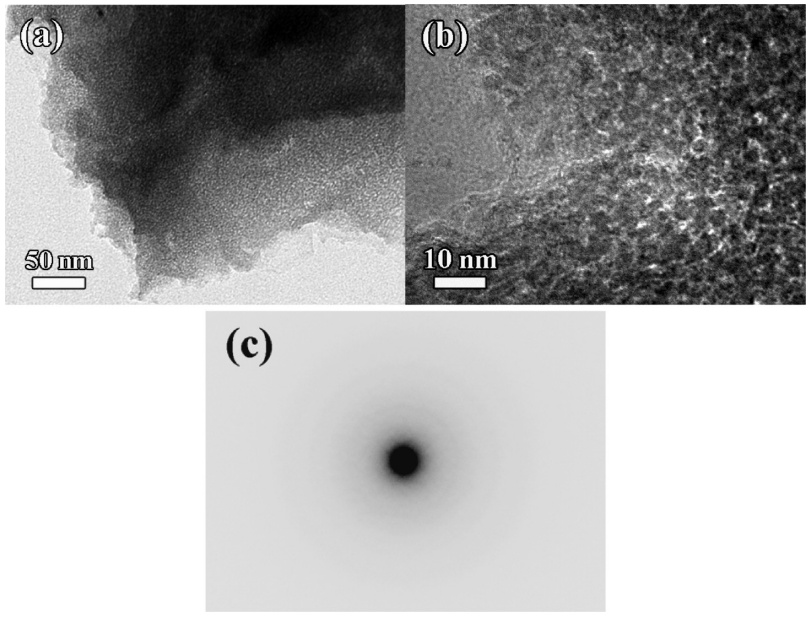

Figure 4. (a, b) TEM images and (c) SAED pattern of the FeOOH/mRGO hybrid.

important tool to study carbonaceous materials. Figure S6 in the Supporting Information shows the Raman spectrum of the FeOOH/mRGO hybrid. Two characteristic peaks are observed at 1351 and 1593 cm^{-1}, consistent with the typical Raman modes of the D band (disordered induced phonon mode) and the G band (graphite band) of carbon, respectively. TG was carried out in air to determine the chemical composition of the bare FeOOH and the FeOOH/mRGO composite (see Figure S7 in the Supporting Information). As shown in Figure S7a in the Supporting Information, the TG curve of the bare FeOOH exhibits a 11.5 wt % weight loss from 250 to 400 °C, which is slightly larger than the theoretical value of the weight change from FeOOH to Fe_2O_3 (10.1 %). Figure S7b in the Supporting Information shows the TG result for the as-formed FeOOH/mRGO hybrid. The weight change between 250 and 700 °C is due to both the decomposition of FeOOH and the combustion of mRGO. Thus, the RGO content in the product is evaluated to be about 31.0 wt %.

Figure 4a shows a typical TEM image of the resulting material. The light contrast can be assigned to the mRGO matrix. In comparison, the dark contrast suggests the FeOOH nanoparticles of higher projected mass density. These extremely tiny nanoparticles of ∼2 nm in size are homogeneously dispersed on the mRGO substrate in a very dense manner almost without aggregation (Figure 4b). The low aggregation suggests that the mRGO nanosheets are important to achieve well-dispersed FeOOH nanoparticles. The corresponding SAED pattern (Figure 4c) indicates that these ultrafine FeOOH nanoparticles are amorphous, which is consistent with the XRD results (Figure 2a).

mRGO plays an important role in the decomposition of iron(III) nitrate and the formation of amorphous FeOOH nanoparticles. As evidenced by the XPS results (Figure 2b−d), the mRGO nanosheets still contain a plenty of functional groups such as −C═O and O−C═O after mild reduction. These mRGO nanosheets could be well dispersed in water due to these oxygen-containing functional groups. During the synthesis process, two main steps are probably included: (a) When Fe^{3+} ions were added into the mRGO suspension, the Fe^{3+} ions were attached to those negatively charged oxygen-containing functional groups through electrostatic interaction. (b) The black mRGO nanosheets absorbed the energy of infrared radiation, which promoted the formation of amorphous FeOOH nanoparticles on the mRGO. Meanwhile, the infrared radiation may help to the further reduction of the oxygen-containing functional groups, thus further improving the conductivity of mRGO. In the control experiments, we also explored the influence of the mRGO and infrared radiation on the formation of amorphous FeOOH nanoparticles. If the mRGO was not utilized or the hybrid was dried at 70 °C instead of infrared radiation, FeOOH nanoparticles cannot be obtained. For the preparation of bare FeOOH, a further heat

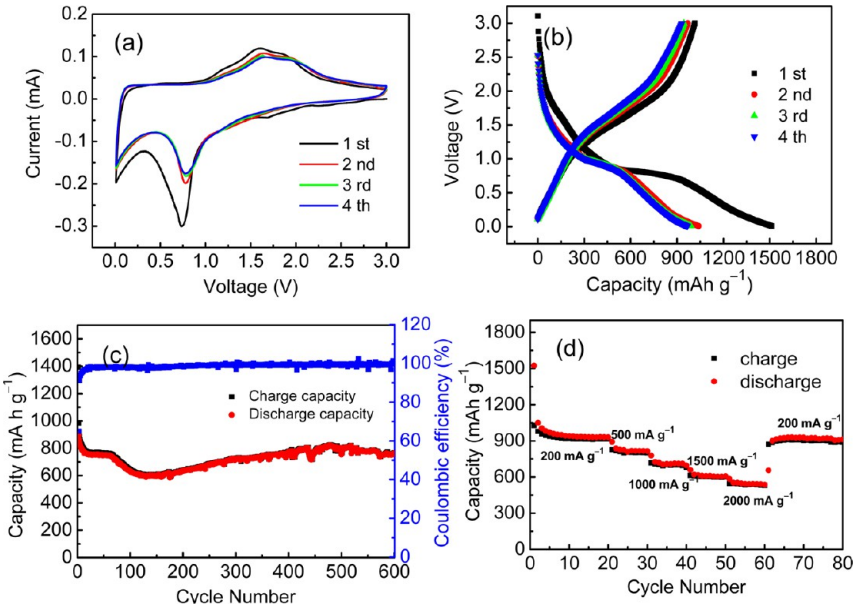

Figure 5. Electrochemical performance of the amorphous FeOOH/mRGO hybrid: (a) CV curves at a scan rate of 0.2 mV s^{-1} in the voltage range of 0.01−3.0 V *vs.* Li^+/Li, (b) discharge/charge curves for the 1st, 2nd, 3rd, and 4th cycles (current density: 200 mA g^{-1}; potential range: 0.01−3 V vs. Li^+/Li), (c) cyclability and coulombic efficiency (current density: 1000 mA g^{-1}; potential range: 0.01−3 V *vs.* Li^+/Li), and (d) capacity over cycling at various current densities of 200, 500, 1000, 1500, and 2000 mA g^{-1} in the voltage range of 0.01−3.0 V vs. Li^+/Li.

treatment at 160 °C for 1 h was needed after infrared radiation (see Figure S8 in the Supporting Information). These results demonstrate that both the mRGO and infrared radiation paly critical roles in the formation of the well-dispersed amorphous FeOOH nanoparticles on mRGO nanosheets. The general reaction for the formation of FeOOH may be simplified as follows

$$Fe(NO_3)_3 + 3H_2O \rightarrow Fe(OH)_3 + 3NO_3^- + 3H^+ \quad (1)$$

$$Fe(OH)_3 \rightarrow FeOOH + H_2O \quad (2)$$

The electrochemical performances of the amorphous FeOOH/mRGO composite were evaluated by CV and galvanostatic discharge−charge cycling. Figure 5a depicts the representative CV curves of the amorphous FeOOH/mRGO hybrid cycled at a scan rate of 0.2 mV s^{-1} in the voltage range of 0.01−3.0 V vs. Li^+/Li. In the first curve, there are three cathodic peaks at around 1.70, 1.20, and 0.75 V, respectively. Meanwhile, two broad peaks at 1.58 and 1.88 V can be observed in the anodic process. The cathodic peaks are ascribed to the Li reaction with FeOOH to produce nanoparticles of Fe embedded in an amorphous matrix of LiOH and Li_2O ($FeOOH + 3Li^+ + 3e^- \rightarrow Fe + LiOH + Li_2O$), while the anodic peaks correspond to the oxidation of Fe nanoparticles into Fe_2O_3 nanoparticles ($2Fe + 3Li_2O \rightarrow Fe_2O_3 + 6Li^+ + 6e^-$).[35] In the second cycle, there is only a slight migration of the main reduction peak (from 0.75 V to 0.78 V), which is different from that of the bare FeOOH (see Figure S9 in the Supporting Information). This phenomenon may result from the enhanced kinetics of the amorphous FeOOH/mRGO hybrid.[45] From the second cycle onward, the reduction peak at about 0.78 V in the cathodic process and the oxidation peaks at about 1.61 and 1.92 V in the anodic scans are clearly observed, and they overlap well with those in the following cycles, indicating the highly reversible reduction and oxidation of the as-prepared material ($Fe_2O_3 + 6Li^+ + 6e^- \leftrightarrow 2Fe + 3Li_2O$).[35] For the bare FeOOH electrode (see Figure S9 in the Supporting Information), similar redox peaks are observed in the first cycle of the CV curves. However, they decline rapidly in the subsequent cycles, indicating the poor reversibility.

Figure 5b shows the discharge/charge curves of the amorphous FeOOH/mRGO hybrid at a current density of 200 mA g^{-1} in the voltage range of 0.01−3.0 V vs. Li^+/Li. In the first curve, there are three obvious voltage plateaus (∼1.70, ∼1.18 and ∼0.78 V vs. Li^+/Li) in the discharge process, corresponding to three lithiation steps,[36] in a good agreement with the CV results. At the same time, there exists a long slope in the low-potential region. The specific capacity corresponding to this region of the first discharge curve may be due to the Li insertion in mRGO.[21] The first charge curve exhibits a long sloped region at ∼1.70 V due to the oxidation reaction of Fe. The as-obtained material delivers a reversible charge capacity of 1015 mA h g^{-1} with a coulombic efficiency of 67.1% in the first cycle. The initial capacity loss may result from the irreversible lithium loss due to the electrolyte decomposition to form a solid electrolyte interphase (SEI) layer and possibly interfacial lithium storage.[46,47] From the second cycle onward, the discharge/charge curves remain steady and reversible, consistent with the CV results. The cycling performance of the amorphous FeOOH/mRGO composite was evaluated at 1000 mA g^{-1} in the voltage range of 0.01−3.0 V vs. Li^+/Li. As shown in Figure 5c, the amorphous FeOOH/mRGO hybrid electrode exhibits extraordinary cyclability with high capacity. A reversible capacity of ∼767 mA h g^{-1} with a coulombic efficiency of ∼100% can be achieved after 600 discharge/charge cycles. Importantly, the amorphous FeOOH/mRGO composite shows excellent rate capability (Figure 5d). Even under the current density as high as 2000 mA g^{-1}, the as-prepared electrode still exhibits a favorable capacity of ∼608 mA h g^{-1}, which is still much higher than the theoretical capacity of graphite (∼372 mA h g^{-1}). Notably, after the measurements at various current densities, the capacity can recover to the initial reversible values, implying good reversibility and very stable cycling performance. In contrast, the electrode made of bare FeOOH

exhibits much worse electrochemical performance, which shows a quick decrease in capacity even at a low current density of 200 mA g^{-1} (Figure 6). The high capacity, good cycling stability and

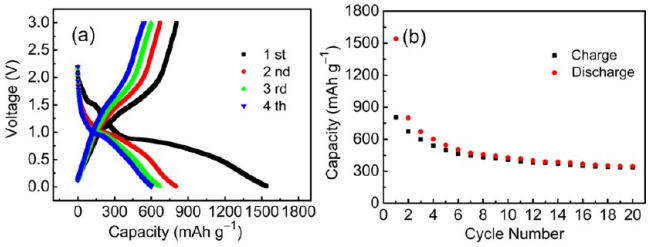

Figure 6. (a) Discharge/charge curves and (b) cycling performance of the bare FeOOH electrode at a current density of 200 mA g^{-1} cycled between the voltage of 3−0.01 V vs. Li/Li^+.

rate capacity of the amorphous FeOOH/mRGO hybrid could be reasonably attributed to the advantageous combination of small FeOOH nanoparticles (~2 nm) with amorphous structure and conductive mRGO. The small primary FeOOH particles render a very short transport length for both lithium ions and electrons upon the discharge/charge cycling. Moreover, the reaction kinetics could be improved due to the amorphous structure.[26] The mRGO nanosheets in the composite can serve as an elastic and highly conductive frame work to maintain the electrical contact from the FeOOH nanoparticles to the current collectors.

The enhanced electrical conductivity of the amorphous FeOOH/mRGO composite was confirmed by EIS (Figure 7).

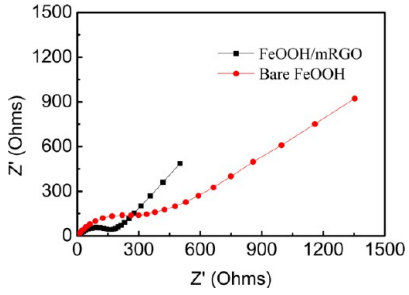

Figure 7. Electrochemical impedance spectra of the FeOOH/mRGO hybrid and bare FeOOH electrodes.

The semi-circle observed in the high and middle frequency range corresponds to the charge transfer resistance at the interface of the composite electrode. The inclined line in the lower frequency, typical of the Warburg impedance, generally reflects the lithium-ion diffusion within the bulk electrode. According to the Nyquist plots of the two samples, the FeOOH/mRGO electrode has a charge transfer resistance value of 160 Ω, which is much smaller than that of the bare FeOOH electrode (450 Ω), revealing a lower charge-transfer resistance in the FeOOH/mRGO composite mainly due to the higher electrical conductivity of the composite. This result indicates that the FeOOH/mRGO electrode possesses a high electrical conductivity, hence resulting in high capacity and good rate capability. To understand the excellent cycling performance of the amorphous FeOOH/mRGO hybrid, the morphology and microstructure variation after cycling were investigated. Figure 8 shows the representative TEM image of the FeOOH/mRGO hybrid after 600 discharge/charge cycles at 1000 mA g^{-1}. It is obviously demonstrated that the FeOOH

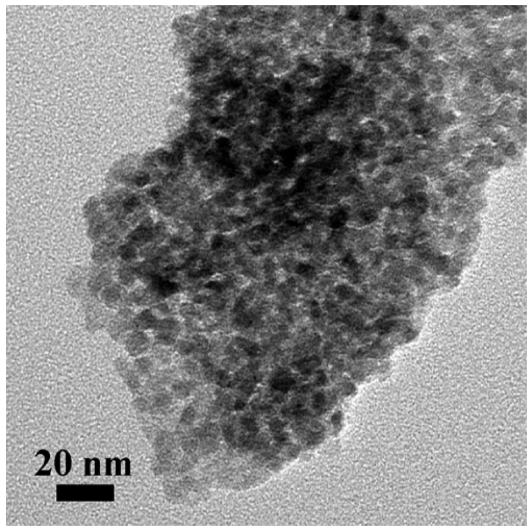

Figure 8. TEM image of the FeOOH/mRGO hybrid after 600 cycles at a current density of 1000 mA g^{-1} cycled between the voltage of 3−0.01 V vs. Li/Li^+.

nanoparticles are still well-dispersed on the mRGO substrate in the initial state even after 600 cycles, indicating good structure stability of the as-prepared composite. Benefiting from the unique composite nanostructure, the strain and stress of the volume change upon cycling could be effectively accommodated, and agglomeration of ultrafine FeOOH nanoparticles is avoided, leading to highly reversible stability. Therefore, the synergetic effect of the small particle size, amorphous structure, and conductive mRGO may contribute to the superior electrochemical performances of the as-prepared FeOOH/mRGO hybrid.

CONCLUSIONS

In summary, we have developed a facile infrared irradiation approach for the synthesis of a unique FeOOH/mRGO nanocomposite, featuring amorphous FeOOH nanoparticles with ~2 nm diameter uniformly grown on the mRGO nanosheets. This method is highly promising for cost-effective and large-scale production. The as-prepared FeOOH/mRGO composite as an anode material exhibits high reversible capacity, excellent cyclability and rate capability, which could be attributed to the enhanced ionic and electronic transport in the electrode. The advantageous combination of the small particle size, amorphous structure and mRGO enables a promising anode material for next-generation high-performance lithium-ion batteries. Moreover, the present synthesis method could be extended to prepare other mRGO-based transition-metal oxide/hydroxide hybrids for lithium-storage applications.

ASSOCIATED CONTENT

Supporting Information

FESEM images, EDX, elemental mapping analyses, Raman spectrum, TG curves, XRD patterns, and CV curves. This material is available free of charge via the Internet at http://pubs.acs.org.

AUTHOR INFORMATION

Corresponding Authors

*Fax: +86-27-87558241. E-mail: huxl@mail.hust.edu.cn.
*E-mail: huangyh@mail.hust.edu.cn.

Notes

The authors declare no competing financial interest.

■ ACKNOWLEDGMENTS

This work was supported by Natural Science Foundation of China (Grants 21271078 and 51002057), PCSIRT (Program for Changjiang Scholars and Innovative Research Team in University), and NCET (Program for New Century Excellent Talents in University, NECT-12-0223). The authors thank Analytical and Testing Center of HUST for the XRD measurements.

■ REFERENCES

(1) Aricò, A. S.; Bruce, P.; Scrosati, B.; Tarascon, J. M.; Schalkwijk, W. V. *Nat. Mater.* **2005**, *4*, 366−377.
(2) Poizot, P.; Laruelle, S.; Grugeon, S.; Dupont, L.; Tarascon, J. M. *Nature* **2000**, *407*, 496−499.
(3) Armand, M.; Tarascon, J. M. *Nature* **2008**, *451*, 652−657.
(4) Li, H.; Wang, Z. X.; Chen, L. Q.; Huang, X. J. *Adv. Mater.* **2009**, *21*, 4593−4607.
(5) Guo, B. K.; Wang, X. Q.; Fulvio, P. F.; Chi, M. F.; Mahurin, S. M.; Sun, X. G.; Dai, S. *Adv. Mater.* **2011**, *23*, 4661−4666.
(6) Ji, L. W.; Lin, Z.; Alcoutlabi, M.; Zhang, X. W. *Energy Environ. Sci.* **2011**, *4*, 2682−2699.
(7) Wang, H. L.; Dai, H. J. *Chem. Soc. Rev.* **2013**, *42*, 3088−3113.
(8) Wu, H.; Chan, G.; Choi, J. W.; Ryu, I.; Yao, Y.; McDowell, M. T.; Lee, S. W.; Jackson, A.; Yang, Y.; Hu, L. B.; Cui, Y. *Nat. Nanotechnol.* **2012**, *7*, 310−315.
(9) Taberna, P. L.; Mitra, S.; Poizot, P.; Simon, P.; Tarascon, J. M. *Nat. Mater.* **2006**, *5*, 567−573.
(10) Sun, Y. M.; Hu, X. L.; Luo, W.; Huang, Y. H. *J. Mater. Chem.* **2012**, *22*, 425−431.
(11) Luo, W.; Hu, X. L.; Sun, Y. M.; Huang, Y. H. *J. Mater. Chem.* **2012**, *22*, 4910−4915.
(12) Xue, D. J.; Xin, S.; Yan, Y.; Jiang, K. C.; Yin, Y. X.; Guo, Y. G.; Wan, L. J. *J. Am. Chem. Soc.* **2012**, *134*, 2512−2515.
(13) Sun, Y. M.; Hu, X. L.; Yu, J. C.; Li, Q.; Luo, W.; Yuan, L. X.; Zhang, W. X.; Huang, Y. H. *Energy Environ. Sci.* **2011**, *4*, 2870−2877.
(14) Sun, Y. M.; Hu, X. L.; Luo, W.; Huang, Y. H. *J. Mater. Chem.* **2012**, *22*, 13826−13831.
(15) Li, X. L.; Wang, X. R.; Zhang, L.; Lee, S. W.; Dai, H. J. *Science* **2008**, *319*, 1229−1232.
(16) Meyer, J. C.; Geim, A. K.; Katsnelson, M. I.; Novoselov, K. S.; Booth, T. J.; Roth, S. *Nature* **2007**, *446*, 60−63.
(17) Dikin, D. A.; Stankovich, S.; Zimney, E. J.; Piner, R. D.; Dommett, G. H. B.; Evmenenko, G.; Nguyen, S. T.; Ruoff, R. S. *Nature* **2007**, *448*, 457−460.
(18) Lee, C.; Wei, X. D.; Kysar, J. W.; Hone, J. *Science* **2008**, *321*, 385−388.
(19) Huang, X.; Qi, X. Y.; Boey, F.; Zhang, H. *Chem. Soc. Rev.* **2012**, *41*, 666−686.
(20) Sun, Y. M.; Hu, X. L.; Luo, W.; Huang, Y. H. *ACS Nano* **2011**, *5*, 7100−7106.
(21) Zhu, X. J.; Zhu, Y. W.; Murali, S.; Stoller, M. D.; Ruoff, R. S. *ACS Nano* **2011**, *5*, 3333−3338.
(22) Sun, Y. M.; Hu, X. L.; Luo, W.; Huang, Y. H. *J. Mater. Chem.* **2011**, *21*, 17229−17235.
(23) Wei, W.; Yang, S. B.; Zhou, H. X.; Lieberwirth, I.; Feng, X. L.; Müllen, K. *Adv. Mater.* **2013**, *25*, 2909−2914.
(24) Wu, Z. S.; Ren, W. C.; Wen, L.; Gao, L. B.; Zhao, J. P.; Chen, Z. P.; Zhou, G. M.; Li, F.; Cheng, H. M. *ACS Nano* **2010**, *4*, 3187−3194.
(25) Wang, X. L.; Han, W. Q.; Chen, H. Y.; Bai, J. M.; Tyson, T. A.; Yu, X. Q.; Wang, X. J.; Yang, X. Q. *J. Am. Chem. Soc.* **2011**, *133*, 20692−20695.
(26) Guo, J. C.; Liu, Q.; Wang, C. S.; Zachariah, M. R. *Adv. Funct. Mater.* **2012**, *22*, 803−811.
(27) Yu, Y.; Yan, C. L.; Gu, L.; Lang, X. Y.; Tang, K.; Zhang, L.; Hou, Y.; Wang, Z. F.; Chen, M. W.; Schmidt, O. G.; Maier, J. *Adv. Energy Mater.* **2013**, *3*, 281−285.
(28) Idota, Y.; Kubota, T.; Matsufuji, A.; Maekawa, Y.; Miyasaka, T. *Science* **1997**, *276*, 1395−1397.
(29) Wang, B.; Chen, J. S.; Wu, H. B.; Wang, Z. Y.; Lou, X. W. *J. Am. Chem. Soc.* **2011**, *133*, 17146−17148.
(30) Wang, Z. Y.; Luan, D. Y.; Madhavi, S.; Hu, Y.; Lou, X. W. *Energy Environ. Sci.* **2012**, *5*, 5252−5256.
(31) Nuli, Y. N.; Zhang, P.; Guo, Z. P.; Liu, H. K. *J. Electrochem. Soc.* **2008**, *155*, A196−A200.
(32) Wang, L. L.; Liang, J. W.; Zhu, Y. C.; Mei, T.; Zhang, X.; Yang, Q.; Qian, Y. *Nanoscale* **2013**, *5*, 3627−3631.
(33) He, C. N.; Wu, S.; Zhao, N. Q.; Shi, C. S.; Liu, E. Z.; Li, J. J. *Acs Nano* **2013**, *7*, 4459−4469.
(34) Amine, K.; Yasuda, H.; Yamachi, M. *J. Power Sources* **1999**, *81*, 221.
(35) Lou, X. M.; Wu, X. Z.; Zhang, Y. X. *Electrochem. Commun.* **2009**, *11*, 1696−1699.
(36) Tabuchi, T.; Katayama, Y.; Nukuda, T.; Ogumi, Z. *J. Power Sources* **2009**, *191*, 636−639.
(37) Zhang, C. M.; Zhu, J. X.; Rui, X. H.; Chen, J.; Sim, D.; Shi, W. H.; Hng, H. H.; Lim, T. M.; Yan, Q. Y. *CrystEngComm* **2012**, *14*, 147−153.
(38) Hummers, W. S.; Offeman, R. E. *J. Am. Chem. Soc.* **1958**, *80*, 1339.
(39) Paek, S. M.; Yoo, E. J.; Honma, I. *Nano Lett.* **2009**, *9*, 72−75.
(40) Moulder, J. F.; Sticlke, W. F.; Sobol, P. E.; Bomben, K. D. *Handbook of X-ray Photoelectron Spectroscopy*; Chastain, J., Ed.; Perkin-Elmer Corporation: Eden Prairie, MN, 1992.
(41) Stankovich, S.; Piner, R. D.; Chen, X. Q.; Wu, N. Q.; Nguyen, S. T.; Ruoff, R. S. *J. Mater. Chem.* **2006**, *16*, 155−158.
(42) Zou, Y. Q.; Wang, Y. *Nanoscale* **2011**, *3*, 2615−2620.
(43) Li, Y. M.; Lv, X. J.; Lu, J.; Li, J. H. *J. Phys. Chem. C* **2010**, *114*, 21770−21774.
(44) Li, F. H.; Song, J. F.; Yang, H. F.; Gan, S. Y.; Zhang, Q. X.; Han, D. X.; Ivaska, A.; Niu, L. *Nanotechnology* **2009**, *20*, 455602.
(45) Delmer, O.; Balaya, P.; Kienle, L.; Maier, J. *Adv. Mater.* **2008**, *20*, 501−505.
(46) Balaya, P.; Li, H.; Kienle, L.; Maier, J. *Adv. Funct. Mater.* **2003**, *13*, 621−625.
(47) Maier, J. *Nat. Mater.* **2005**, *4*, 805−815.